ORIGINAL PAPER

Tao Wu · Tong Chen · Hui Yan · Jianjun Qu

Modeling analysis and tuning of shunt piezoelectric damping controller for structural vibration

Abstract When the passive control technology is used to control the bending vibration of flexible structures, the shunt piezoelectric damping technology is commonly regarded as a straightforward and efficient approach. However, its performance is sensitive to the changes of the components' parameter values on the piezoelectric transducer, and usually requires more accurate tuning. This study introduces a novel optimization algorithm and criteria to optimize the parameters of the components in the shunt piezoelectric damping circuit. Specifically, the evaluation criteria for suppressing bending vibration are formulated using the frequency response and kinetic energy power spectrum. The improved Sine Cosine Algorithm (SCA) is then employed to optimize the parameters of the frequently used parallel, series, and negative capacitance impedance circuits. The accuracy of the model is verified by comparing the derived dynamic model and transfer function model with the results obtained from finite element software Workbench. Subsequently, the system's response is analyzed under different parameter values, damping conditions, and excitations. The convergence and feasibility of the improved SCA algorithm are demonstrated through an example that involves suppressing the bending vibration of a rectangular plate. Furthermore, the optimization calculation of component parameter values in the example circuit is conducted, and the results are compared with those obtained through previous methods, thereby affirming the effectiveness and advantages of the proposed algorithm for optimizing component parameter values in shunt piezoelectric damping circuits.

1 Introduction

Shunt piezoelectric damping is a technology that converts the mechanical energy of the controlled system into electrical energy using the piezoelectric effect of the piezoelectric material bonded to the host structure, and then dissipates it through an external circuit. This technology is widely favored for mitigating structural vibrations due to its ability to obviate the necessity of incorporating dampers, which may introduce considerable mass to the mechanical structure, or elastic materials that can have a substantial impact on the overall volume. Furthermore, this technology can be implemented without the need for an additional power source. Nevertheless, the effectiveness of shunt piezoelectric damping is highly dependent on the component parameters within the external electrical network, which makes it sensitive to variations in these parameters. Moreover, different controlled systems may necessitate different parameters for the transducer and induction elements [1–3]. Consequently, optimizing and fine-tuning the components in the transducer circuit becomes imperative to achieve optimal vibration suppression performance. Some researchers have also summarized the previous research achievements and technical challenges associated with shunt damping technology [4–7].

T. Wu (✉) · H. Yan · J. Qu
School of Mechatronics Engineering, Harbin Institute of Technology, Harbin, People's Republic of China
e-mail: 19b908099@stu.hit.edu.cn

T. Chen
College of Engineering, University of Michigan, Ann Arbor, USA

In the existing research, various combination modes have been employed for external electrical networks in shunt piezoelectric damping systems. These modes typically include single resistance, series connection of inductance and resistance, parallel connection of inductance and resistance, and the utilization of negative capacitance [8, 9]. Researchers have explored parameter selection and circuit optimization techniques for these external electrical networks in order to achieve broader control frequency bands, improved control effectiveness, and enhanced reliability [10–12]. For instance, Zhao [13] developed a hybrid shunt piezoelectric circuit that integrates both passive and active circuit components. Through simulations, it was demonstrated that this circuit exhibits superior vibration suppression performance compared to pure passive or active control approaches. In order to improve the control performance and avoid wasting the driving power, Ji et al. [14] proposed a new method to realize asymmetric bipolar voltage by using the negative capacitance shunt circuit. This method involved the addition of a resistor and a diode to the negative capacitance circuit, enabling the generation of asymmetric bipolar voltages. Considering the practical challenges in adjusting the capacitance ratio between the negative capacitance and the inherent capacitance of the piezoelectric transducer, Pohl [15] introduced the concept of an adaptive negative capacitance circuit and derived the transfer function of the regulation rule. In a related study, Berardengo et al. [16] proposed and experimentally validated a novel circuit configuration for vibration suppression, consisting of a pair of negative capacitors. The results demonstrated the superiority of this circuit arrangement compared to configurations utilizing a single capacitor. In terms of model calculation and solution, Soltani et al. [17] recognized that it was approximate to apply fixed points of equal height in the receiving transfer function in the previous method, and then deduced the exact closing solution when the inductance and resistance were connected in parallel. Ducarne et al. [18] investigated the free response and forced response of the mechanical structure using the semi-analytical model, enabling them to accurately determine the response time of the system. Ravi and Zilian [19] proposed a hybrid finite element formulation for the predictive modeling and simulation of piezoelectric energy harvesting devices. Their holistic approach ensures consistent solutions for structural dynamics in coupled fields and accounts for the electromechanical effects of piezoelectric materials. Yamada et al. [20] deduced the system vibration suppression equation based on the principle of force balance. Through their analysis, they determined the optimal values of parameters for LR circuits connected in series and parallel configurations. To enhance the accuracy of the lumped-parameter model of transverse vibration, Wang and Lu [21] introduced a correction factor that accounts for the dynamic vibration mode shape and strain distribution. This correction factor enables the derivation of steady-state expressions for both electrical and mechanical responses under excitation at any frequency. The above researchers have optimized the shunt piezoelectric damping system in terms of external electrical network and model solution, respectively.

Several researchers have focused on tuning the parameter values of components in the fundamental external electrical network. For instance, Raze et al. [2] introduced a novel sequential tuning procedure that imposes passivity constraints on each controlled mode and enables quantitative selection of control authority from the outset. To address interference between two modes, Høgsberg and Krenk [22] proposed an explicit calibration method for series and parallel RL circuits, striking makes a compromise between frequency response and control amplitude. Gardonio et al. [23] presented a self-tuning method based on the maximization of vibrational power dissipation. This method estimates the electrical power dissipated by each shunt and optimizes the vibrational power dissipation of its resonant response within the target frequency range through tuning. Beck et al. [24] refined the parameter values of the components in the external shunt circuit by minimizing the induced voltage resulting from substrate vibration. This novel tuning method was experimentally validated to ensure its effectiveness. Toftekær et al. [25] utilized the built-in capabilities of commercial finite element software to derive a general formula for calibrating parallel RL circuits. This approach enables effective control of multiple vibration modes tailored to specific plate vibration issues. Heuss et al. [26] introduced a combined tuning method that incorporates the traditional tuning mass absorber while considering the strong influence of shunt piezoelectric ceramics. Through simulations and experiments, they demonstrated the effectiveness of this method in accurately predicting the behavior of electromechanical systems. Lumentut and Howard [27] employed the extended Hamilton principle to model the shunt circuit behavior of the piezoelectric control layer. They further optimized system parameters using an adaptive tuning strategy, resulting in significant improvements in system performance.

This paper presents a new optimization algorithm and optimization criteria to tune the parameters of components in the external electrical network of piezoelectric transducers. Firstly, the dynamic model and transfer function model of electromechanical coupling system are derived in detail, and the model is truncated and reduced. Furthermore, several enhancements are made to the Sine Cosine Algorithm [28] to improve the global search ability and local development accuracy of the algorithm. Finally, examples are provided to
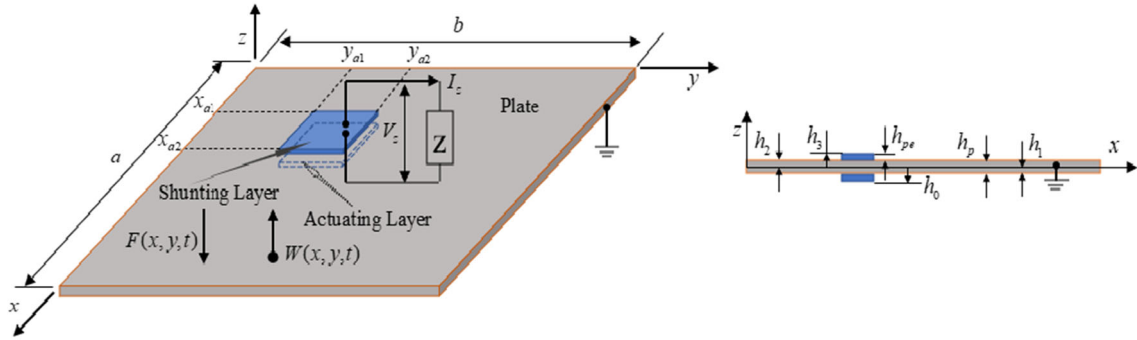
Fig. 1 Plate with shunted piezoelectric patch and actuated piezoelectric patch

optimize the three commonly used piezoelectric shunt circuits, and compared with the methods mentioned by previous researchers to verify the effectiveness of the algorithm.

2 Modelling equations

In this section, the dynamic model of a rectangular plate with piezoelectric patches attached under the consideration of electromechanical coupling will be introduced first. Subsequently, detailed derivations of the frequency response formula and transfer function formula are provided. Additionally, a novel criterion for optimizing the parameter values of the shunt piezoelectric damping circuit is introduced. Lastly, several enhancements are incorporated into the SCA algorithm to augment both its global search capability and local convergence accuracy.

2.1 Electromechanical coupling dynamic model

As depicted in Fig. 1, a thin piezoelectric transducer is integrated onto a rectangular plate with dimensions of length a and width b. The rectangular plate is assumed to be composed of an isotropic material, while the transducer is fabricated using piezoelectric ceramics polarized in the z direction and exhibiting isotropy within the xy plane. The integration between the transducer and the rectangular plate is assumed to be seamless.

Consider a rectangular plate with piezoelectric transducers and simply supported on four sides, its vibration differential equation can be expressed as:

$$D\left(\frac{\partial^4 w(x,y,t)}{\partial x^4} + 2\frac{\partial^4 w(x,y,t)}{\partial x^2 \partial y^2} + \frac{\partial^4 w(x,y,t)}{\partial y^4}\right) + \rho_p h_p \frac{\partial^2 w(x,y,t)}{\partial t^2}$$

$$+\xi_p \frac{\partial w(x,y,t)}{\partial t} = K_a\left(\frac{\partial^2 R}{\partial x^2} + \frac{\partial^2 R}{\partial y^2}\right) \tag{1}$$

where $D = E_p h_p^3 \big/ 12(1 - v_p^2)$ is the bending stiffness; E_p, v_p, ρ_p, h_p are, respectively, the Young's modulus, Poisson's ratio, density and thickness of the rectangular plate; M_x and M_y are defined as the moment per unit length that drives the piezoelectric element along the x and y directions; ξ_p is the modal damping ratio of the rectangular plate; K_a is the characteristic parameter of the coupling between the rectangular plate and the piezoelectric element, K_a and $R(x, y)$ can be expressed as:

$$K_a = \frac{d_{31}}{h_{pe}} V_a K^f \tag{2}$$

$$R(x, y) = [H(x - x_{a1}) - H(x - x_{a2})][H(y - y_{a1}) - H(y - y_{a2})] \tag{3}$$

where (x_{a1}, y_{a1}) and (x_{a2}, y_{a2}) are the coordinates of the lower left corner and upper right corner of the driving element; $H(\cdot)$ is the Heaviside function; V_a is the driving voltage of the driving piezoelectric element; d_{31} is

the strain constant; h_{pe} is the thickness of the piezoelectric element; K^f is a geometric constant related to the properties of the piezoelectric element and the rectangular plate, and K^f can be shown as:

$$K^f = -\frac{E_P h_p^2}{6} \frac{1 + \nu_{pe}}{1 - \nu_p} \frac{p}{1 + \nu_p - (1 + \nu_{pe})p} \quad (4)$$

$$P = -\frac{1}{2} \frac{E_{pe}}{E_P} \frac{1 - \nu_P^2}{1 - \nu_{pe}^2} \frac{6h_{pe}h_p(h_{pe} + h_p)}{h_p^3 + 8h_{pe}^3 + 6h_p h_{pe}^2} \quad (5)$$

where E_{pe}, ν_{pe} and h_{pe}, respectively, represent Young's modulus, Poisson's ratio and thickness of piezoelectric element; $w(x, y, t)$ represent transverse displacement of the rectangular plate, which can be written in the form of a combination of time and space variables:

$$w(x, y, t) = \sum_{m=1}^{\infty} \sum_{n=1}^{\infty} \phi_{mn}(x, y)\eta_{mn}(t) = \Phi(x, y)\eta(t) \quad (6)$$

where $\phi_{mn}(x, y)$ is the natural mode function of the plate without considering the coupling effect of the piezoelectric transducer and the rectangular plate, which can be defined as $\phi_{mn}(x, y) = \frac{2}{\sqrt{ab}} \sin(m\pi x/a) \sin(n\pi y/b)$, and $\eta_{mn}(t)$ is the generalized coordinate function of the transverse vibration of the rectangular plate. In addition, it can be obtained:

$$\frac{\partial^2 R}{\partial x^2} + \frac{\partial^2 R}{\partial y^2} = -\sum_{m=1}^{\infty} \sum_{n=1}^{\infty} \frac{2}{\sqrt{ab}} \left(\frac{mb}{na} + \frac{na}{mb}\right) \phi_{mn}(x, y) \left(\cos\frac{m\pi x_{a1}}{a} - \cos\frac{m\pi x_{a2}}{a}\right)$$
$$\times \left(\cos\frac{n\pi y_{a1}}{b} - \cos\frac{n\pi y_{a2}}{b}\right) \quad (7)$$

The expression for the voltage generated by the shunt piezoelectric can be written as [29]:

$$V_{out}(t) = \frac{h_p + h_{pe}}{2C_{pe}} \int_{y_{a1}}^{y_{a2}} \int_{x_{a1}}^{x_{a2}} \left(e_{31}\frac{\partial^2 w}{\partial x^2} + e_{32}\frac{\partial^2 w}{\partial y^2} + 2e_{36}\frac{\partial^2 w}{\partial x \partial y}\right) \mathrm{d}x\mathrm{d}y \quad (8)$$

where e_{31}, e_{32}, e_{36} are the stress constants of piezoelectric materials. In the shunt piezoelectric system described in this paper, $e_{36} = 0$, $e_s = e_{31} = e_{32}$. Substituting Eq. (6) into Eq. (8), the voltage generated by shunt piezoelectricity can be expressed as follows:

$$V_{out}(t) = -\frac{e_s}{\sqrt{ab}C_{pe}}(h_p + h_{pe})$$
$$\times \sum_{m=1}^{\infty} \sum_{n=1}^{\infty} \left(\frac{mb}{na} + \frac{na}{mb}\right)\left(\cos\frac{m\pi x_{a1}}{a} - \cos\frac{m\pi x_{a2}}{a}\right)\left(\cos\frac{n\pi y_{a1}}{b} - \cos\frac{n\pi y_{a2}}{b}\right)\eta_{mn}(t) \quad (9)$$

Under the simply supported boundary condition, the natural frequency of the rectangular plate can be determined by solving the following equation:

$$\omega_{mn} = \sqrt{\frac{D}{\rho_p h_p}\left[\left(\frac{m\pi}{a}\right)^2 + \left(\frac{n\pi}{b}\right)^2\right]} \quad (10)$$

By employing the modal expansion method to expand the displacement function described in Eq. (6), the electromechanical coupling equation of the piezoelectric energy harvester working around its natural frequency can be obtained [30]:

$$\mathbf{M}\ddot{\eta}(t) + \mathbf{C}_p\dot{\eta}(t) + \mathbf{K}\eta(t) - \mathbf{\Theta}_{pe}V_z(t) = \mathbf{F}_{ext}(t) \quad (11)$$

$$\mathbf{\Theta}_{pe}\eta(t) - C_{pe}V_z(t) = -q_{pe}(t) \quad (12)$$

where $q_{pe}(t)$ is the charge generated on the piezoelectric transducer, and the current on the shunt circuit can be obtained as $I_z = \mathrm{d}q_{pe}(t)/\mathrm{d}t$; $V_z(t)$ is the voltage generated on the piezoelectric components; $\mathbf{M}$ and $\mathbf{K}$ are, respectively, the electromechanical coupling mass matrix and stiffness matrix; $\mathbf{C_P}$ is the system damping

matrix considering modal damping; $\boldsymbol{\Theta}_{pe}$, C_{pe} and $\mathbf{F}_{ext}(t)$ are, respectively, the electromechanical coupling matrix, the capacitance and force of the piezoelectric components. Assuming that there are N_{pe} piezoelectric elements pasted on the rectangular plate, the above parameters can be obtained:

$$\mathbf{M} = \int_{S_P} \rho_p h_p \boldsymbol{\Phi}(x,y)^T \boldsymbol{\Phi}(x,y) \mathrm{d}S_P + \sum_{i=1}^{N_{pe}} \int_{S_{\mathrm{pe}.i}} \rho_{pe} h_{pe} \boldsymbol{\Phi}(x,y)^T \boldsymbol{\Phi}(x,y) \mathrm{d}S_{\mathrm{pe}.i} \tag{13}$$

$$\mathbf{K} = \int_{h_1}^{h_2} h^2 \mathrm{dh} \int_{S_{pe}} \boldsymbol{\Phi}''(x,y)^T \tilde{C}_p \boldsymbol{\Phi}''(x,y) \mathrm{d}S_p$$

$$+ \sum_{i=1}^{N_{pe}} \int_{h_0}^{h_1} h^2 \mathrm{dh} \int_{S_{\mathrm{pe}.i}} \boldsymbol{\Phi}''(x,y)^T \tilde{C}_{pe}^E \boldsymbol{\Phi}''(x,y) \mathrm{d}S_{\mathrm{pe}.i} \tag{14}$$

$$\boldsymbol{\Theta}_{pe} = \sum_{i=1}^{N_{pe}} \int_{h_0}^{h_1} \frac{h}{h_{\mathrm{pe}}} \mathrm{dh} \int_{S_{\mathrm{pe}.i}} \boldsymbol{\Phi}''(x,y)^T \boldsymbol{e}_{\mathrm{pe}} \mathrm{d}S_{\mathrm{pe}.i} \tag{15}$$

$$\mathbf{C}_p = 2\xi_p \rho_p h_p \sqrt{\frac{\mathbf{K}}{\mathbf{M}}} \int_{S_P} \boldsymbol{\Phi}(x,y)^T \boldsymbol{\Phi}(x,y) \mathrm{d}S_P \tag{16}$$

$$C_{\mathrm{pe}.i} = \int_{S_{\mathrm{pe}.i}} \rho_{\mathrm{pe}} h_{\mathrm{pe}} \varphi(y)^T \varepsilon^s \varphi(y) \mathrm{d}S_{\mathrm{pe}.i} \tag{17}$$

where ρ_{pe} represents the density of the piezoelectric element; S_p and S_{pe} represent the upper surface area of the rectangular plate and the piezoelectric element, respectively; $\tilde{C}_p$ represents the elastic modulus of the material of the rectangular plate; $\tilde{C}_{\mathrm{pe}}^E$ represents the elastic modulus of the piezoelectric material (measured under a constant electric field); $\mathbf{e}_{\mathrm{pe}}$ represents the piezoelectric coupling coefficient; ε^s represents the dielectric constant of the piezoelectric material, and $\varphi(y)$ represents the electric field function in the thickness direction.

In Fig. 1, the piezoelectric element is connected to an external circuit for shunting, characterized by an impedance of $Z(s)$. The relationship between the impedance and the voltage and current can be expressed as follows:

$$V_z(s) = I_z(s)Z(s) \tag{18}$$

where $I_z(s)$ and $V_z(s)$ are, respectively, the current flowing through the shunt impedance and the voltage across the impedance. By applying Kirchhoff's law, the voltage $V_{\mathrm{pe}}(s)$ generated across the piezoelectric element and the internal impedance $Z_{\mathrm{pe}}(s)$ of the piezoelectric element are substituted into Eq. (18). This substitution yields the following equation:

$$V_z(s) = V_{\mathrm{pe}}(s) - Z_{\mathrm{pe}}(s)I_z(s) \tag{19}$$

It is generally considered that the internal impedance of the piezoelectric element is $Z_{\mathrm{pe}}(s) = {}^1\!/_{C_{\mathrm{pe}}s} + R_{\mathrm{pe}}$, and in the ideal case, the dielectric loss can be ignored, that is, $Z_{\mathrm{pe}}(s) = {}^1\!/_{C_{\mathrm{pe}}s}$ [31]. By substituting Eq. (18) into Eq. (19), the following equation can be derived:

$$V_{\mathrm{pe}}(s) = V_z(s) + \frac{Z_{\mathrm{pe}}(s)}{Z(s)} V_z(s) \tag{20}$$

In the frequency domain, the total impedance of the piezoelectric element and the external shunt circuit can be expressed as follows:

$$Z_{ppe}(\omega) = \frac{Z(\omega)}{1 + j\omega Z(\omega)C_{\mathrm{pe}}} \tag{21}$$

where the external impedance $Z(\omega)$ is related to the connection method of the external circuit. In this paper, three common basic shunt circuits are mainly studied, namely the parallel circuit of inductance and resistance,

the series circuit of inductance and resistance, and the series circuit of negative capacitance and resistance. The frequency-domain expressions for the corresponding impedances of these three circuits are as follows:

$$
Z(\omega) = \begin{cases} \frac{j\omega RL}{R+j\omega L} & \text{R and L in parallel} \\[2mm] R + jwL & \text{R and L in series} \\[2mm] -\frac{1}{j\omega C} + R & \text{C and R in series} \end{cases} \tag{22}
$$

where R, L and C, respectively, represent the magnitude of resistance, inductance and capacitance.

2.2 Transfer function model of composite system

In the electromechanical coupled system depicted in Fig. 1, comprising piezoelectric elements and rectangular plates, external excitations can originate from concentrated forces, displacements, or laterally uniformly distributed forces. These external excitations can be converted into disturbance voltages acting on the system. Assuming the system is subjected to a voltage disturbance of magnitude $V_{\mathrm{dis}}(s)$, and considering the presence of an external impedance with a finite magnitude:

$$
V_{\mathrm{pe}}(s) = G_{vv}(s)V_{\mathrm{dis}}(s) - G_{vv}\frac{Z(s)}{Z(s) + Z_{\mathrm{pe}}(s)}V_{\mathrm{pe}}(s) \tag{23}
$$

where $G_{vv}(s)$ is the open-loop transfer function from the shunt piezoelectric output voltage $V_{\mathrm{out}}(s)$ to the driving piezoelectric voltage $V_a(t)$.

By sorting out Eq. (23), it can be obtained:

$$
\overline{G}_{vv}(s) = \frac{V_{\mathrm{pe}}(s)}{V_{\mathrm{dis}}(s)} = \frac{G_{vv}(s)}{1 + G_{vv}G_H(s)} \tag{24}
$$

where $\overline{G}_{vv}(s)$ represents the transfer function of the closed-loop system, while $G_H(s) = Z(s)\big/(Z(s) + Z_{\mathrm{pe}}(s))$ denotes the feedback link. Similarly, the closed-loop transfer function between the displacement of a point and the interference voltage can also be obtained:

$$
\overline{G}_{wv}(s) = \frac{W(x, y, s)}{V_{\mathrm{dis}}(s)} = \frac{G_{wv}(s)}{1 + G_{vv}G_H(s)} \tag{25}
$$

where $G_{wv}(s)$ is the closed-loop transfer function from the displacement of a point to the interference voltage in the open-loop state.

By substituting Eqs. (6) and (7) into Eq. (1), it can be obtained:

$$
\ddot{\eta}_{mn}(t) + 2\zeta_{mn}\omega_{mn}\dot{\eta}_{mn}(t) + \omega_{mn}^2\eta_{mn}(t) = -\frac{2}{\sqrt{ab}\rho_p h_p}\frac{K^f d_{31}}{h_{pe}}\left(\frac{mb}{na} + \frac{na}{mb}\right)
$$
$$
\times \left(\cos\frac{m\pi x_{a1}}{a} - \cos\frac{m\pi x_{a2}}{a}\right)\left(\cos\frac{n\pi y_{a1}}{b} - \cos\frac{n\pi y_{a2}}{b}\right)V_a(t) \tag{26}
$$

By multiplying both sides of Eq. (26) by $\phi_{mn}(x, y)$, followed by performing Laplace transform and rearranging the terms, the closed-loop transfer function from the displacement of a specific point in the open-loop state to the driving voltage can be obtained:

$$
G_{wv}(s) = \frac{W(x, y, s)}{V_a(s)} = -\frac{2}{\sqrt{ab}\rho_p h_p}\sum_{m=1}^{\infty}\sum_{n=1}^{\infty}\frac{\phi_{mn}(x, y)\psi_{mn}}{s^2 + 2\zeta_{mn}\omega_{mn}s + \omega_{mn}^2} \tag{27}
$$

where

$$
\psi_{mn} = \frac{K^f d_{31}}{h_{pe}}\left(\frac{mb}{na} + \frac{na}{mb}\right)\left(\cos\frac{m\pi x_{a1}}{a} - \cos\frac{m\pi x_{a2}}{a}\right)\left(\cos\frac{n\pi y_{a1}}{b} - \cos\frac{n\pi y_{a2}}{b}\right) \tag{28}
$$

Similarly, by utilizing Eq. (9), Eq. (1), Eq. (6) and Eq. (27), the open-loop transfer function from the shunt piezoelectric output voltage $V_{out}(s)$ to the driving voltage $V_a(t)$ can be derived:

$$G_{vv}(s) = \frac{V_{\text{out}}(s)}{V_a(s)} = \frac{2e_s}{ab\rho_p h_p} \frac{h_p + h_{pe}}{C_{pe}} \sum_{m=1}^{\infty} \sum_{n=1}^{\infty} \frac{\psi_{mn} Q_{mn}}{s^2 + 2\zeta_{mn}\omega_{mn}s + \omega_{mn}^2} \tag{29}$$

where

$$Q_{mn} = \left(\frac{mb}{na} + \frac{na}{mb}\right)\left(\cos\frac{m\pi x_{a1}}{a} - \cos\frac{m\pi x_{a2}}{a}\right)\left(\cos\frac{n\pi y_{a1}}{b} - \cos\frac{n\pi y_{a2}}{b}\right) \tag{30}$$

In the process of practical application, it is not necessary to consider all frequency ranges but only the relevant frequency ranges associated with the actual vibration. Therefore, employing an infinite order model as described in Eqs. (27) and (29) is not appropriate. Hence, the aforementioned transfer functions need to be truncated and reduced in order to obtain a more practical representation:

$$\tilde{G}_{wv}(s) \triangleq \frac{W(x, y, s)}{V_a(s)} = -\frac{2}{\sqrt{ab}\rho_p h_p} \sum_{m=1}^{M} \sum_{n=1}^{N} \frac{\phi_{mn}(x, y)\psi_{mn}}{s^2 + 2\zeta_{mn}\omega_{mn}s + \omega_{mn}^2} + K_{opt}^w \tag{31}$$

$$\hat{G}_{vv}(s) \triangleq \frac{V_s(s)}{V_a(s)} = \frac{2e_s}{ab\rho_p h_p} \frac{h_p + h_{pe}}{C_{pe}} \sum_{m=1}^{M} \sum_{n=1}^{N} \frac{\psi_{mn} Q_{mn}}{s^2 + 2\zeta_{mn}\omega_{mn}s + \omega_{mn}^2} + K_{opt}^v \tag{32}$$

where K_{opt}^w and K_{opt}^v represent the correction terms that arise from the truncation of the transfer function. These correction terms can be determined using the methodology outlined in reference [31].

In Eq. (11), the harmonic displacement variable of the coupled vibration between the rectangular plate and the piezoelectric material can be substituted with $f(t) = f(\omega)\exp(j\omega t)$, where $f(\omega)$ represents the complex amplitude and ω denotes the angular frequency. The following equation can be obtained [32]:

$$\left[-\omega^2 \mathbf{M} + j\omega(\mathbf{C}_p + Z_{ppe}\boldsymbol{\Xi}_{pe}) + \mathbf{K}\right]\boldsymbol{\eta}(\omega) = \mathbf{F}(\omega) \tag{33}$$

where the piezoelectric coupling matrix $\boldsymbol{\Xi}_{pe} = \boldsymbol{\Theta}_{pe}\boldsymbol{\Theta}_{pe}^T$. For the ith order natural frequency of the system, the transfer function of displacement and force in the generalized coordinates can be written as follows:

$$G_{\eta f} = \frac{\eta_i}{F_i} = \frac{1}{-\omega^2 M_i + j\omega(C_{p.i} + Z_{ppe}(\omega)\Xi_{pe.i}) + K_i} \tag{34}$$

2.3 Optimization criteria

When employing the shunt piezoelectric damping method to control the vibration of a thin plate, the vibration energy of the system can be effectively dissipated by designing the appropriate circuit and optimizing its parameters. During the design and optimization process, the reduction of amplitude or energy is commonly used as the optimization criterion. In this study, the effectiveness of optimization is evaluated using the frequency response and the power spectrum of kinetic energy. Assuming that the displacement of the thin plate in the frequency domain is denoted as $\mathbf{W}(x, y, \omega)$, the following equation can be derived by combining Eq. (33):

$$\boldsymbol{\eta}(\omega) = \mathbf{W}(x, y, \omega)\mathbf{F}(\omega) \tag{35}$$

and then it can be obtained:

$$\mathbf{W}(x, y, \omega) = \frac{j\omega}{-\omega^2 \mathbf{M} + j\omega(\mathbf{C}_p + Z_{ppe}(\omega)\boldsymbol{\Xi}_{pe}) + \mathbf{K}} \tag{36}$$

According to reference [32], the power spectral density of the system can be expressed as:

$$S_K(\omega) = \frac{1}{2}Tr\left[\mathbf{M}\mathbf{W}(x, y, \omega)\delta(x - x')\delta(y - y')\mathbf{W}^H(x, y, \omega)\right] \tag{37}$$

where $Tr[\cdots]$ is the trace operation of the matrix, and $\delta(\cdot)$ is the Dirac function; (x, y) and (x', y') represent the respective positions associated with the cross-spectral density for uncorrelated and randomly distributed transverse forces acting on the thin plate.

Assuming that $[\omega_1, \omega_2]$ is the frequency range of interest, the average kinetic energy power spectral density of the system is:

$$\overline{S}_K = \frac{\sum_{\omega_1}^{\omega_2} S_K(\omega)}{\omega_2 - \omega_1} \tag{38}$$

Furthermore, the unit sinusoidal sweep frequency interference voltage can be applied to the piezoelectric driving element to obtain the displacement response of the system. The average frequency response of the system can be expressed as follows:

$$\overline{S}_G = \frac{\sum_{\omega_1}^{\omega_2} \left| \tilde{G}_{wv}(s) \right|}{\omega_2 - \omega_1} \tag{39}$$

Then the cost function for optimizing the parameter values of each component in the shunt piezoelectric damping circuit can be defined as:

$$J = \min\left\{ \frac{\overline{S}_{K.NC}}{\overline{S}_{K.NC} - \overline{S}_{K.C}} \right\} \quad \text{or} \quad J = \min\left\{ \frac{\overline{S}_{G.NC}}{\overline{S}_{G.NC} - \overline{S}_{G.C}} \right\} \tag{40}$$

where the subscript "NC" denotes the absence of control, indicating that the external circuit is open, and the subscript "C" denotes the presence of the shunt piezoelectric damping circuit for control.

2.4 Improved optimization algorithm

The Sine Cosine Algorithm (SCA) is a meta-heuristic algorithm that leverages the periodic oscillation of sine and cosine functions to facilitate global exploration and local exploitation. Initially introduced by Mirjalili in 2015 for airfoil design [28], the SCA algorithm belongs to the family of swarm intelligence algorithms. It employs a random solution set as the initial population and utilizes an iterative strategy along with an objective evaluation function to iteratively update and explore the solution space. Research has demonstrated that the SCA algorithm exhibits superior search performance compared to certain other intelligent algorithms. Moreover, the SCA algorithm is characterized by its simpler structure, requiring fewer parameter settings and easier implementation [33]. The original SCA algorithm mainly includes the following steps:

(a) Initialize the candidate solution space $\mathbf{U}$: Create a candidate solution by setting N variables, where each candidate solution has a decision dimension of D. Initialize the candidate solutions as follows:

$$\mathbf{U} = \begin{bmatrix} \mathbf{U}_1 \\ \mathbf{U}_2 \\ \vdots \\ \mathbf{U}_n \end{bmatrix} = \begin{bmatrix} x_1^1 \, x_1^2 \, \cdots \, x_1^d \\ x_2^1 \, x_2^2 \, \cdots \, x_2^d \\ \vdots \, \vdots \, \vdots \, \vdots \\ x_n^1 \, x_n^2 \, \cdots \, x_n^d \end{bmatrix} \tag{41}$$

where n represents the number of candidate solutions; d represents the dimension of a single solution; $\mathbf{U}_i = (x_i^1, x_i^2, \ldots, x_i^d)$ represents the ith candidate solution, and x_i^j represents the component of the ith solution in the jth dimension.

(b) Calculate the fitness of the candidate solution: Compute the objective function value for each candidate solution to determine its fitness. Store the candidate solution with the highest fitness value as the current optimal candidate solution $P(t)$.

(c) Update algorithm parameters:$r1$ and $r2$ in the algorithm control the step size and direction of updating the current solution to the current optimal solution, which affects whether the current solution is located in the solution space between the current solution and the optimal solution or in the space outside.$r2$ is a random number subject to uniform distribution, $r2 \in [0, 2\pi]$, the update formula of $r1$ is as follows:

$$r1 = a \cdot \left(1 - \frac{t}{T} \right) \tag{42}$$

where $a = 2$, t is the number of current iterations, and T is the maximum number of iterations.

(a) Change trends of $r1$ and   (b) Decreasing pattern for range of sine and cosine
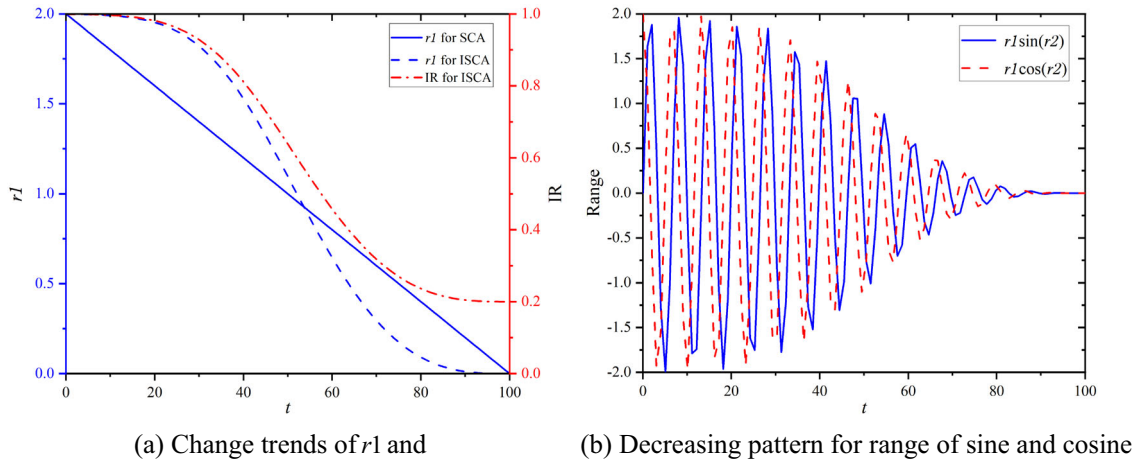
Fig. 2 Variation relevant of related parameters during iteration

(d) Update the candidate solution: Update each candidate solution using appropriate formulas to maintain diversity in the solution space. The update formula for each variable in the candidate solution can be expressed as follows:

$$x_i^j(t+1) = \begin{cases} x_i^j(t) + r1 \cdot \sin(r2) \cdot \left| r3 \cdot P^j(t) - x_i^j(t) \right|, r4 > 0.5 \\ x_i^j(t) + r1 \cdot \cos(r2) \cdot \left| r3 \cdot P^j(t) - x_i^j(t) \right|, r4 \leq 0.5 \end{cases} \tag{43}$$

where $r3$ is the weight of the current optimal solution and represents the influence of the optimal solution on the current solution; $r4$ describes the randomness of using sine or cosine to update the solution.

Although the original Sine Cosine Algorithm (SCA) has demonstrated certain advantages in terms of random search capability, adaptability, and stability, it is susceptible to local optima and premature convergence for certain optimization problems. Moreover, the algorithm exhibits significant fluctuations around the optimal solution, necessitating further enhancements to its convergence. This paper aims to improve the SCA algorithm's global search capability and local development accuracy by optimizing it in the following aspects.

(a) From Eq. (43), it is evident that the sine and cosine parameters $r1\sin(r2)$ and $r1\cos(r2)$ play a crucial role in the global search and local development capabilities of the algorithm. Meanwhile, $r2$ influences the direction of solution updates, and $r1$ determines the step size in the iterative process, representing the rate of distance towards the final solution. The update strategy for $r1$ significantly impacts the algorithm's search capability and convergence. Upon examining Eqs. (42) and (43), it becomes apparent that as the algorithm progresses, $r1 < 1$ remains true, causing the algorithm to primarily focus on local development rather than global search, thereby increasing the likelihood of obtaining local optima. Additionally, the rate at which $r1$ converges to 0 greatly affects the algorithm's precision and accuracy. Consequently, a $r1$ update scheme is devised to strike a balance between global search, local development, and tail convergence:

$$r1 = a \cdot \left(\log(2) - \log\left(1 + \exp\left(-\left(2 \times \left(\frac{T-t}{T} \right) \right)^3 \right) \right) \right) \tag{44}$$

Figure 2 illustrates the fluctuation curve of $r1$ and the fluctuation path of $r1\sin(r2)$ and $r1\cos(r2)$ before and after the proposed improvement. In Fig. 2a, it is observed that the improved $r1$ sustains a substantial value during the initial stages and rapidly diminishes towards 0 during the later stages. This behavior ensures the preservation of population diversity during the early stages of the algorithm while facilitating solution convergence during the later stages.

(b) In the optimization of nature-inspired heuristic algorithms, the concept of inertia weight plays a crucial role as it characterizes the degree of inheritance of candidate solutions from the previous generation's solution space. Previous studies have indicated that the inertia weight significantly impacts the overall

Table 1 Dimensions and physical parameters of the plate and PZT patches

Parameter	Value	
	Plate	PZT patches
$a \times b$ (length $\times$ width)	0.8 m $\times$ 0.6 m	0.1 m $\times$ 0.1 m
h (Thickness)	1×10^{-3} m	0.2×10^{-3} m
E (Young's modulus)	2.1×10^{11} Pa	6.9×10^{10} Pa
ρ (Density)	7870 kg$/$m^3	7700 kg$/$m^3
ν (Poisson ratio)	0.3	0.3
e_s (Stress constant)	$\cdots$	6.2 C$/$m^2
C (Capacitance)	$\cdots$	6.3×10^{-7} F
ζ (Damping ratio)	0.005	$\cdots$

convergence speed in intelligent optimization algorithms. In this study, a linear function is employed to implement a time-varying inertia weight:

$$\eta(t) = \eta_{\max} - t \times \frac{\eta_{\max} - \eta_{\min}}{T} \tag{45}$$

where $\eta(t)$ is the inertia weight of the tth iteration; $\eta_{\max}$ and $\eta_{\min}$ are the maximum inertia weight and the minimum inertia weight, respectively.

(c) To mitigate the volatility around the optimal solution during the later stage of the SCA algorithm and enhance the likelihood of updating and exchanging candidate solutions, an interaction factor IR is introduced. The iterative update of IR is defined as follows:

$$\text{IR} = \text{IR}_{\max} - \delta \times \log\left(1 + \exp\left(-\left(2 \times \frac{T - t}{T}\right)^3\right)\right) \tag{46}$$

Figure 2a shows the IR fluctuation curve when $\text{IR}_{\max}=1$ and $\delta=1.1542$. The optimized candidate solution update formula is as follows:

$$x_i^j(t+1) = \begin{cases} \eta(t)x_i^j(t) + r1 \cdot \sin(r2) \cdot \left| r3 \cdot P^j(t) - x_i^j(t) \right| & r4 > 0.5, r5 < IR \\ \eta(t)x_i^j(t) + r1 \cdot \cos(r2) \cdot \left| r3 \cdot P^j(t) - x_i^j(t) \right| & r4 \leq 0.5, r5 < IR \\ x_i^j & r5 \geq IR \end{cases} \tag{47}$$

In Eq. (47), $r5$ represents a random number ranging from 0 to 1. As observed from the equation, an increase in IR leads to more frequent updates and exchanges among candidate solutions. Figure 2a and Fig. 2b demonstrate that during the early iterations, IR is often greater than the expected value of the random number $r5$ with a high probability. This characteristic ensures a favorable update probability for candidate solutions and enhances the global search capability of the algorithm. Furthermore, as the iteration progresses, there is a high likelihood that the IR becomes lower than the random number $r5$, ensuring the accuracy of the mining algorithm in subsequent stages while reducing its volatility.

3 Numerical examples and discussions

In this section, the derived model will be validated using finite element simulation software Workbench to ensure its accuracy. Subsequently, response analysis will be performed on the developed model under various parameter values, damping conditions, and excitations. Furthermore, the improved SCA algorithm will be employed to optimize and analyze the component parameters of three commonly used shunt piezoelectric damping circuits: parallel inductance and resistance, series inductance and resistance, and series negative capacitance and resistance. The obtained results will be compared with those of previous researchers. The calculation process will involve the utilization of the parameters listed in Table 1.

Table 2 Comparison of the natural frequencies of the analytical method and finite element method

Mode	Analytical method (Hz)	FEM method (Hz)	Error (%)
(1,1)	10.7668	10.606	1.49
(2,1)	22.3320	22.122	0.94
(1,2)	31.3215	31.128	0.62
(3,1)	41.5451	41.342	0.49
(2,2)	42.9549	42.816	0.32
(3,2)	62.4294	62.346	0.13
(1,3)	65.9927	65.234	1.15
(4,1)	69.4850	68.302	1.70

3.1 Calculation and verification of the model

The model takes into account the effect of attaching piezoelectric material to the rectangular plate surface, which causes a shift in the natural frequency of the system in the open-loop state. To verify the accuracy of the model, the calculated results are compared with those obtained from finite element software. Table 2 presents the results, where the coordinates of the center point of the attached piezoelectric material are (0.3 m, 0.25 m), and other parameters are provided in Table 1. The finite element method was implemented using the solid226 element in Workbench, with a mesh size of 0.01 m and a quadrilateral mesh division.

It can be seen from Table 2 that the maximum error percentage between the first eight natural frequencies of the system calculated by the method described in this paper and the natural frequencies obtained by the finite element software simulation is 1.7%, which is within an acceptable range and verifies the accuracy of the obtained stiffness matrix and mass matrix.

By combining Eqs. (26), (9), (6) and (1), and neglecting the effects of modal damping, the transverse displacement of the rectangular plate resulting from applying voltage to the driving piezoelectric layer under static conditions, as well as the voltage generated by the shunt piezoelectric layer, can be determined as follows:

$$w(x, y) = -\frac{2}{\sqrt{ab\rho_p h_p}} \sum_{m=1}^{M} \sum_{n=1}^{N} \frac{\phi_{mn}(x, y)\psi_{mn}}{\omega_{mn}^2} V_a \tag{48}$$

$$V_{\text{out}} = \frac{2e_s}{ab\rho_p h_p} \frac{h_p + h_{pe}}{C_{pe}} \sum_{m=1}^{M} \sum_{n=1}^{N} \frac{\psi_{mm} Q_{mn}}{\omega_{mn}^2} V_a \tag{49}$$

Considering the application of a unit voltage to the piezoelectric driving layer, and placing the piezoelectric elements at points where x_{a1} is equally distributed and y_{a1} is equal to 0.1 m, 0.3 m, and 0.4 m, respectively, the displacement results of the rectangular plate obtained using Eq. (48) are compared with those obtained using finite element software. The comparison results are presented in Fig. 3a. Additionally, Fig. 3b displays the comparison results of the voltages of the shunt piezoelectric layers when the piezoelectric sheet is pasted at the position of (0.25 m, 0.2 m) and voltage values ranging from 2 to 20 V are applied to the driving layer. It can be observed from Fig. 3 that the static displacement response and shunt piezoelectric voltage response obtained by applying the interference voltage align with the results obtained from the finite element simulation software, thereby confirming the accuracy of the relevant derivations.

The closed-loop transfer function from the displacement of a point to the driving voltage and the open-loop transfer function from the shunt piezoelectric output voltage to the driving piezoelectric voltage are shown in Eqs. (27) and (29), respectively. To validate the accuracy of these transfer functions, the first five-order frequency responses of the system are computed using the equations provided in this paper and the frequency response analysis method in Workbench. The obtained results are presented in Fig. 4.

From Fig. 4, it is evident that the frequency response data obtained using the derived transfer function in this paper aligns well with the data obtained from the finite element simulation software. This successful match confirms the accuracy of the derived transfer function, thereby establishing a foundation for optimizing the parameter values of the components in the subsequent paragraphs.
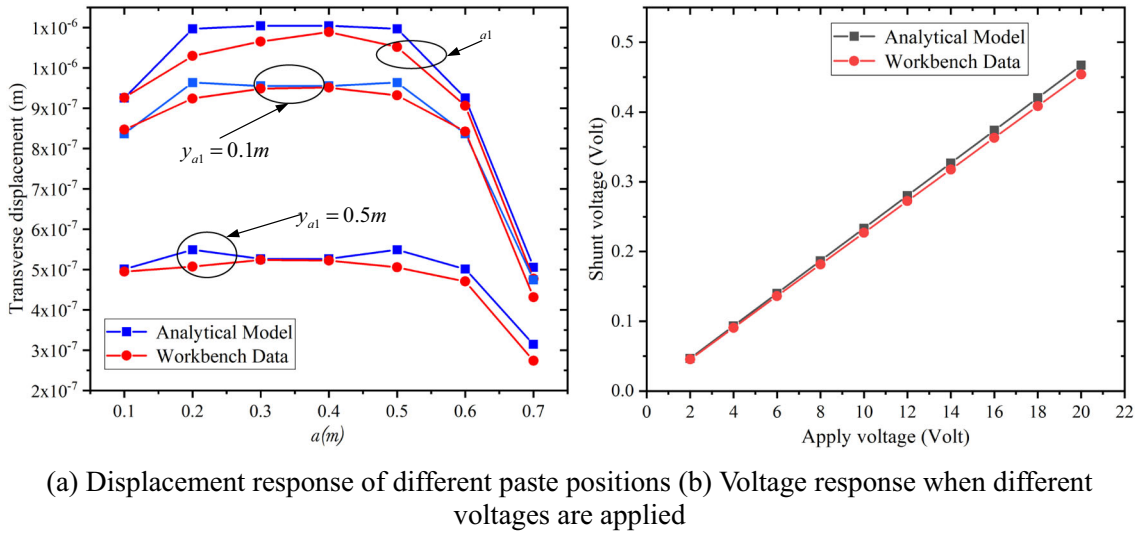
(a) Displacement response of different paste positions (b) Voltage response when different voltages are applied

Fig. 3 Static displacement and voltage response

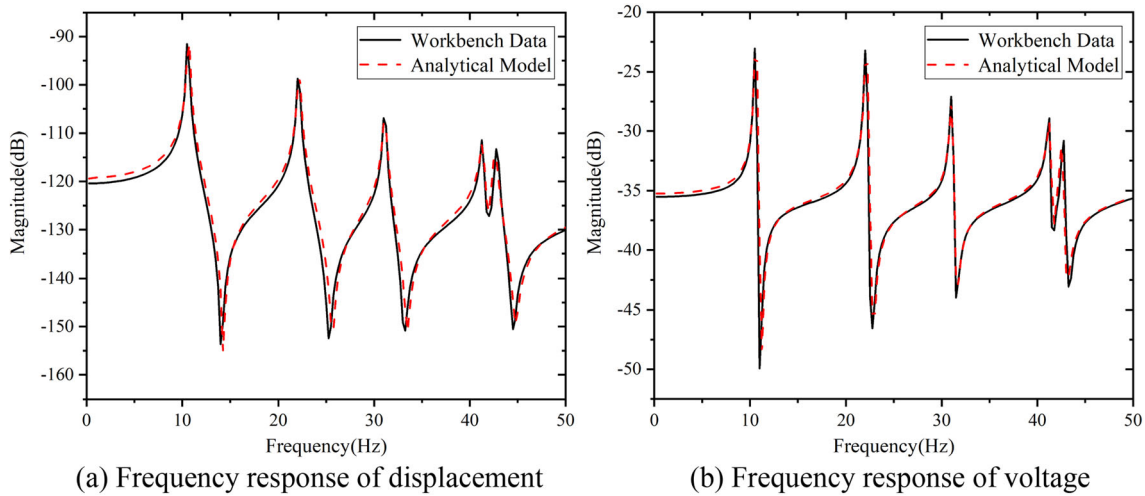(a) Frequency response of displacement   (b) Frequency response of voltage

Fig. 4 Comparison of frequency response between analytical model and Workbench simulation

3.2 Transfer function analysis

It should be noted that Eqs. (27) and (29) utilize infinite-order models, which can result in tedious calculations and potentially become computationally infeasible due to their high order in practical applications. Therefore, in this paper, a truncated form with a finite number of terms is adopted, along with a correction term. Figure 5 displays the frequency response outcomes for different truncation orders without the correction term. As depicted in Fig. 5a, b, while the poles of the truncated system align correctly, the zeros deviate from their correct positions. As the closed-loop performance of the system heavily relies on the positions of the open-loop zeros, it is crucial to ensure that the zeros are as close to their correct positions as possible. Figure 5 demonstrates that the correction term can accomplish this objective effectively.

Subsequently, the impact of modal damping on the displacement and voltage responses is investigated. The piezoelectric element is centrally attached at the coordinates (0.3 m, 0.25 m), and a unit voltage is applied. Through simulation, the displacement and voltage responses of the transfer function are obtained for various modal damping parameters, as depicted in Fig. 6. Observing Fig. 6, it is evident that as the modal damping coefficient gradually increases, the amplitudes of the displacement and voltage responses progressively decrease. This observation aligns with our intuitive understanding.
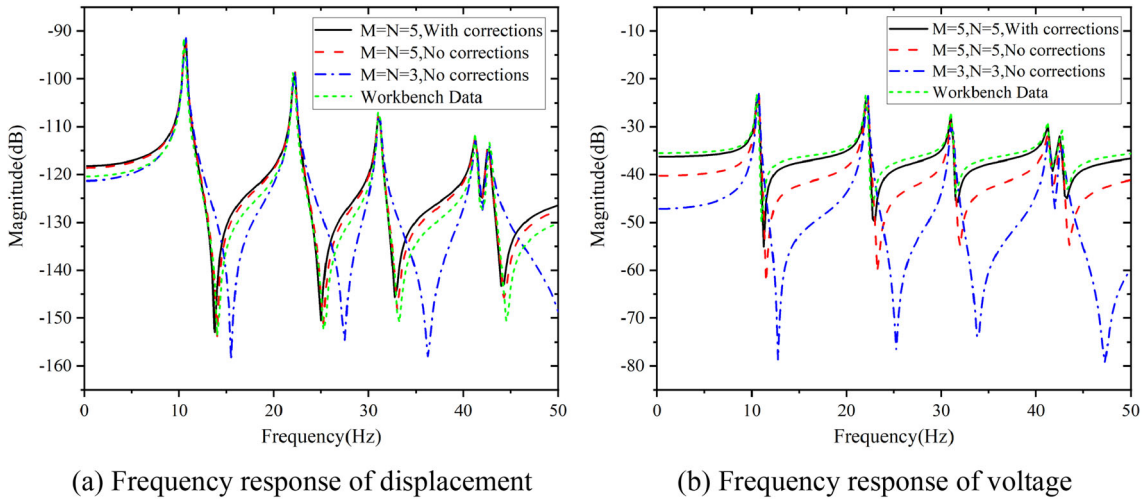
(a) Frequency response of displacement (b) Frequency response of voltage

Fig. 5 Frequency response comparison between with and without correction items

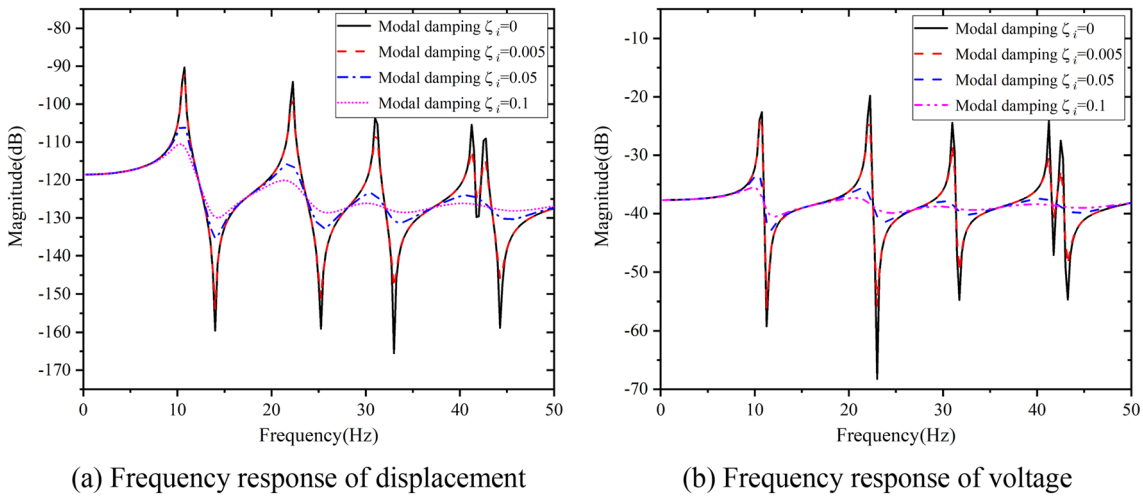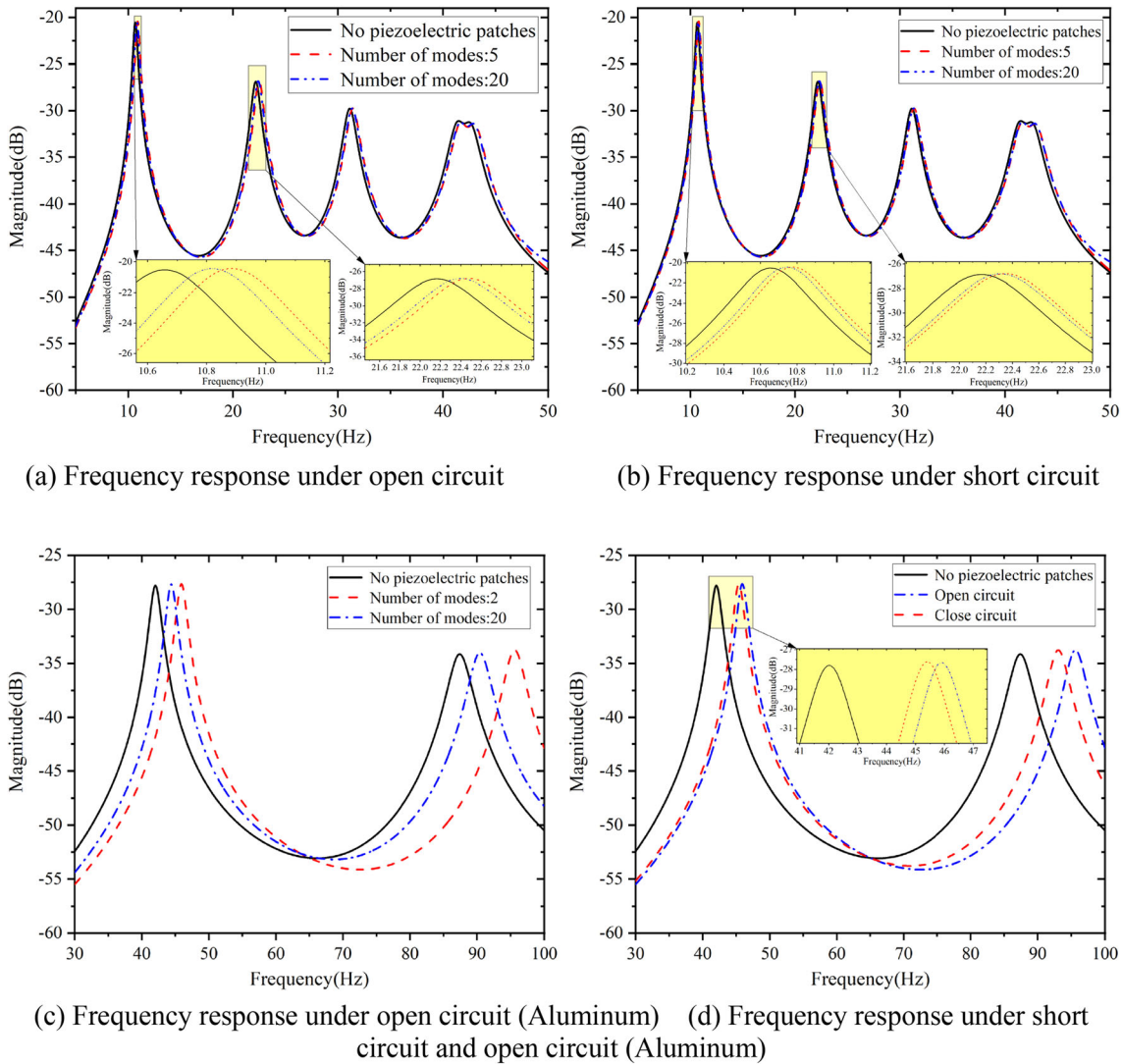(a) Frequency response of displacement (b) Frequency response of voltage

Fig. 6 Frequency response under different modal damping coefficients

The impact of the number of modes considered in Eq. (37) on the frequency response of the system under open-circuit and short-circuit conditions is investigated. Figure 7a, b adopt the parameters specified in Table 1. As illustrated in Fig. 7a, b, the resonance peaks in the open-circuit and short-circuit states shift towards higher frequencies. As the number of selected modes increases, the resonance peaks progressively approach the position where no piezoelectric sheet is attached. Additionally, the resonance peaks in the open-circuit and short-circuit states exhibit a general similarity. This example demonstrates that the number of selected modes has a certain influence on the resonance peaks under open-circuit and short-circuit conditions, indicating a relationship with mode superposition. The slight disparity between Fig. 7a, b can be attributed to the chosen material parameters. To further investigate this, the material of the plate is changed to aluminum, and the length and width of the plate are reduced to half of their original values. The resulting frequency responses under open-circuit and short-circuit conditions are depicted in Fig. 7c, d. Figure 7c, d exhibit more pronounced shifts in the resonance peaks, indicating that the geometric and material properties of the plate have a certain impact on mode superposition.

(a) Frequency response under open circuit   (b) Frequency response under short circuit

(c) Frequency response under open circuit (Aluminum)   (d) Frequency response under short circuit and open circuit (Aluminum)

Fig. 7 Compare the frequency response of the system under different modal orders

3.3 Shunt tuning

Prior to commencing shunt tuning on the circuit, it is imperative to analyze the improved SCA algorithm. Figure 8 illustrates the utilization of both the SCA algorithm and the improved SCA algorithm to search for the minimum values of the two objective functions, as specified in reference [28]. The algorithm settings used were consistent with those in reference [28], and the theoretical analysis suggests that the minimum values of the two objective functions should be 0. Observing Fig. 8, it becomes evident that the improved SCA algorithm exhibits improved convergence speed and accuracy when compared to the original SCA algorithm, thereby affirming the effectiveness of the improved approach. Furthermore, reference [28] provides comparative results between the SCA algorithm and other intelligent algorithms.

During the application of shunt piezoelectric damping for structural vibration control, various connection methods exist for the shunt circuit. The fundamental circuit configurations include parallel connection of inductance (L) and resistance (R), series connection of inductance (L) and resistance (R), and series connection of negative capacitance (C) and resistance (R). Each of these circuit forms requires specific parameter optimization for the external components as the optimal values vary according to the chosen circuit configuration. Hence, it is essential to conduct dedicated parameter optimization for different circuit configurations.
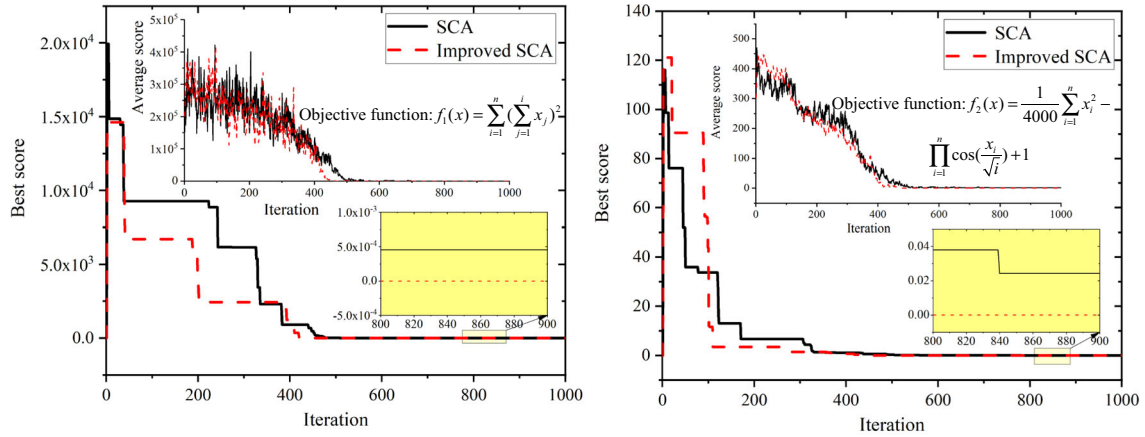
(a) Curve of average fitness and best fitness   (b) Curve of average fitness and best fitness

Fig. 8 Comparison of convergence and accuracy between SCA algorithm and improved SCA algorithm

(a) When the external circuit consists of inductance (L) in parallel with resistance (R), the optimal values for resistance and inductance can be obtained as described in reference [32] through the following equations:

$$R_{\mathrm{opt}} = \sqrt{\frac{M_{11}}{\Xi_{11}C_{pe}}}, L_{\mathrm{opt}} = \frac{M_{11}}{K_{11}C_{pe}} \tag{50}$$

(b) When the external circuit consists of inductance (L) connected in series with resistance (R), the optimal values for resistance and inductance can be obtained as described in reference [32] through the following equations:

$$\begin{cases} L_{\mathrm{opt}} = \dfrac{2M_{11}K_{11}C_{pe}+M_{11}\Xi_{11}}{4K_{11}C_{pe}\Xi_{11}+2\Xi_{11}^2+2K_{11}^2C_{pe}^2} \\ \\ R_{\mathrm{opt}} = \sqrt{\dfrac{(2K_{11}C_{pe}\Xi_{11}+\Xi_{11}^2+K_{11}^2C_{pe}^2)L_{\mathrm{opt}}^2+M_{11}^2-(2M_{11}K_{11}C_{pe}+M_{11}\Xi_{11})L_{\mathrm{opt}}}{M_{11}C_{pe}\Xi_{11}+M_{11}K_{11}C_{pe}^2}} \end{cases} \tag{51}$$
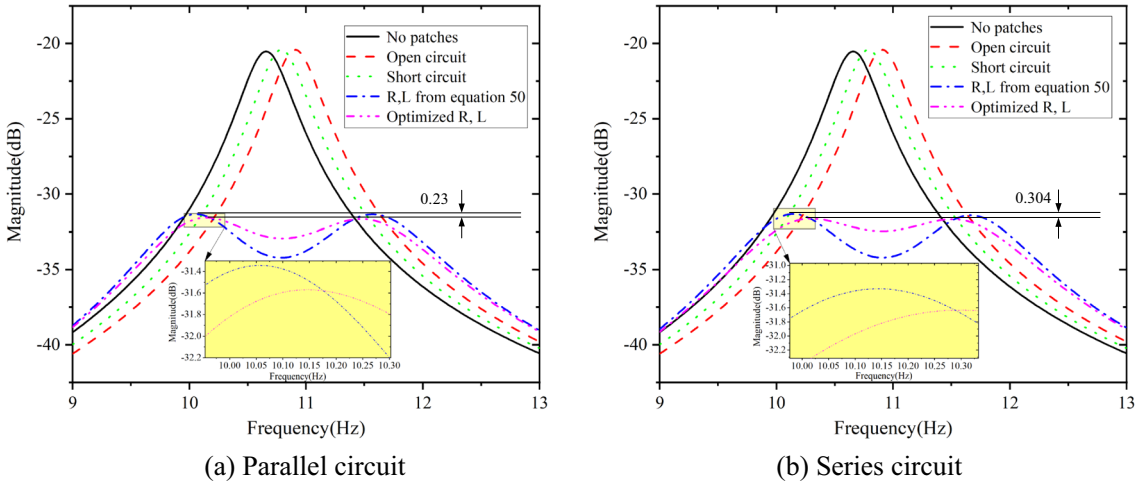
First, the improved SCA algorithm is employed to optimize the parameter values when the inductance and resistance are connected in parallel. Through the optimization process, the optimal values for inductance (L) are determined to be 345H, and the optimal resistance (R) is determined to be 129,125 Ω. Figure 9 illustrates the changes in parameters during the optimization process. It can be observed that both the resistance (R) and inductance (L) gradually converge to specific values, validating the convergence and feasibility of the improved SCA algorithm.

Considering the first-order modal vibration, the parameter values for resistance (R) and inductance (L) are determined using Eq. (50) and the improved SCA algorithm for both the series and parallel systems. For the series system, the optimized values are determined as $L_{opt} = 333$H and $R_{opt} = 4454\Omega$. As described above, the optimization results for the parallel system are also obtained. Figure 10 presents the comparison results of the reduction in the first-order modal vibration kinetic energy achieved by these two optimization algorithms. From Fig. 10, it can be observed that the parameters obtained through the improved SCA algorithm result in a greater reduction in the system's vibration kinetic energy.

Figure 11 presents the contour map depicting the reduction in system vibration kinetic energy for various combinations of inductance and resistance values, considering the first-order modal vibration. The marked points in the plot signify the optimal combination of inductance and resistance values achieved through the utilization of contour plots, improved SCA algorithms, and Eq. (50), respectively. The visualization in Fig. 11 indicates that adopting component parameter values falling within the red area leads to the maximum reduction in system kinetic energy. Moreover, the component parameter values obtained via the improved SCA algorithm exhibit a closer proximity to those derived from the contour map (the observed discrepancy could potentially

(a) Changes in average and best scores   (b) The trajectory of the optimization variable
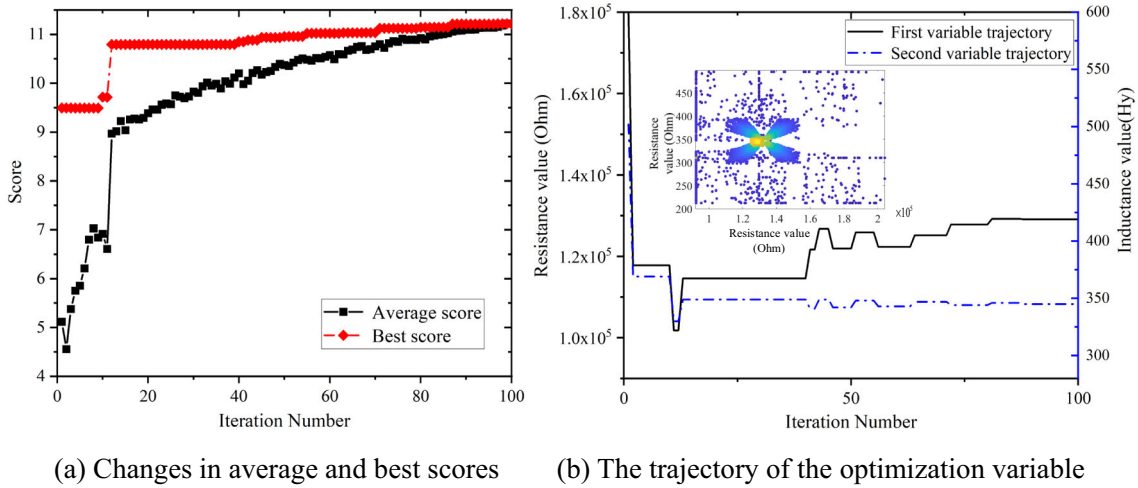
Fig. 9 The SCA algorithm optimizes the value of parallel resistance R and inductance L

(a) Parallel circuit   (b) Series circuit

Fig. 10 Comparison of system kinetic energy reduction considering the first-order mode

be attributed to the discretization interval employed during the construction of the contour map). This further attests to the reliability of the optimization outcomes.

Subsequently, the influence of multi-modal coupling is investigated by considering the first three-order, first five-order, and first eight-order modal couplings of the system under both parallel and series configurations of inductance and resistance. Equation (50) and the improved SCA algorithm are employed to optimize the parameter values of inductance and resistance. The obtained parameter values are then applied to the circuit, and a comparison of the system's vibration reduction is conducted, as illustrated in Fig. 12. From Fig. 12, it is evident that the parameter values obtained through the improved SCA algorithm exhibit a more pronounced effect in suppressing system vibration as the number of mode couplings increases. This finding underscores the superior performance of the optimized parameter values in mitigating the effects of multi-modal coupling on the system's vibration.

Taking into account the coupling of the eight-order modes, the parameter values of inductance and resistance are kept constant, while the parameter values of other components are varied to determine the relative amplitude reduction of the system compared to the open-circuit state. The results are presented in Fig. 13. From Fig. 13, it is evident that the maximum reduction in system amplitude occurs at the optimal values of resistance and inductance. This finding highlights the critical role played by these parameter values in achieving the highest degree of amplitude reduction in the system.

The series connection of a negative capacitor and a resistor is considered, and the optimized capacitance $C_{\mathrm{opt}} = 6.4 \times 10^{-7}$ F and resistance $R_{\mathrm{opt}} = 135\Omega$ are obtained using the improved SCA algorithm. Figure 14a
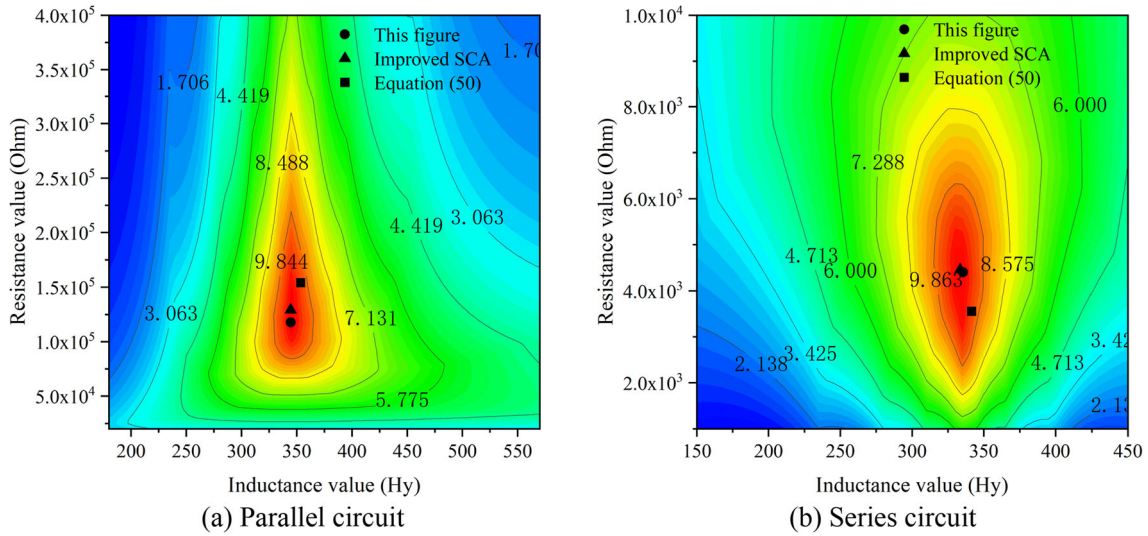
(a) Parallel circuit (b) Series circuit

Fig. 11 Reduction of kinetic energy of the system with different values of R and L

(a) First 3 order modal coupling (b) First 5 order modal coupling (c) First 8 order modal coupling

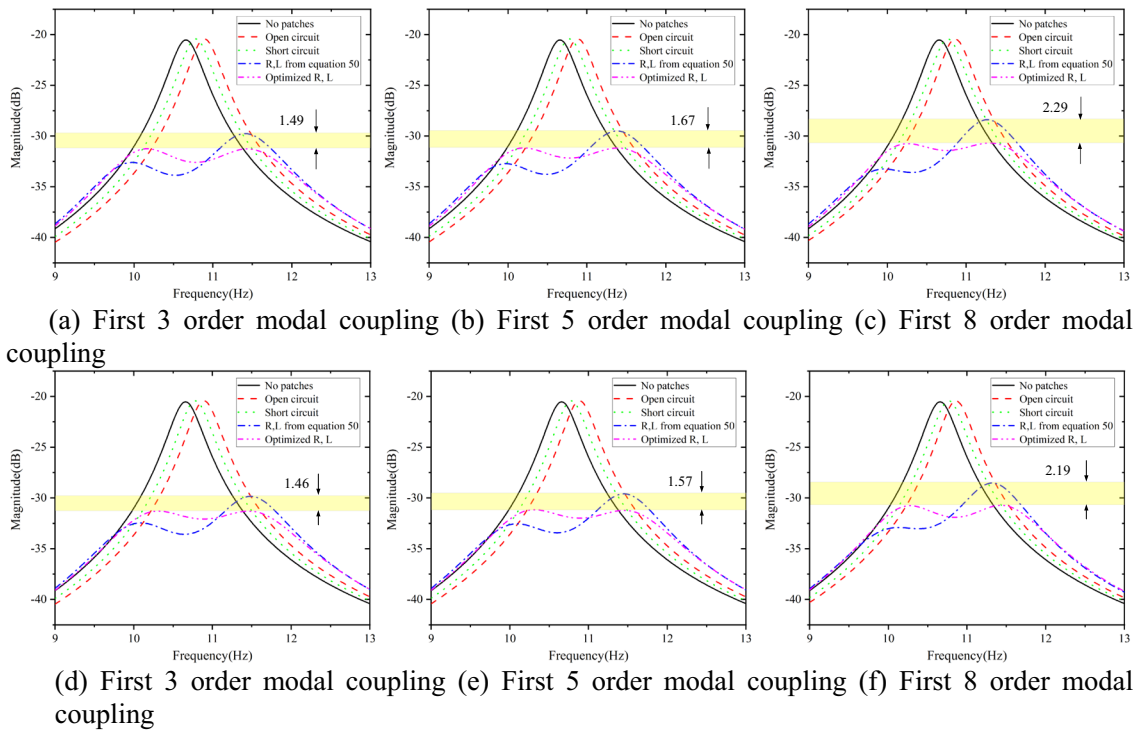(d) First 3 order modal coupling (e) First 5 order modal coupling (f) First 8 order modal coupling

Fig. 12 Comparison of the vibration attenuation of the R and L optimized by the existing method and the method in this paper in the circuit considering different number of modal couplings. **a–c** are obtained from the parallel circuit, and **e–f** are obtained from the series circuit

illustrates the reduction in system vibration achieved by employing the series circuit with the negative capacitor and resistor. From Fig. 14a, it can be observed that in the first five modes, the modal amplitude of the system is reduced by at least 4.2 dB. Additionally, the vibration of the fourth and fifth modes, which have close frequencies, is effectively controlled. This indicates that the series circuit with negative capacitance and resistance exhibits a significant inhibition effect on the vibration of the system with densely spaced modes. Figure 14b demonstrates that the optimized parameters further shift the system's poles to the left. This shift indicates an increased damping in the mechanical system, thereby enhancing the vibration suppression effect of the system.
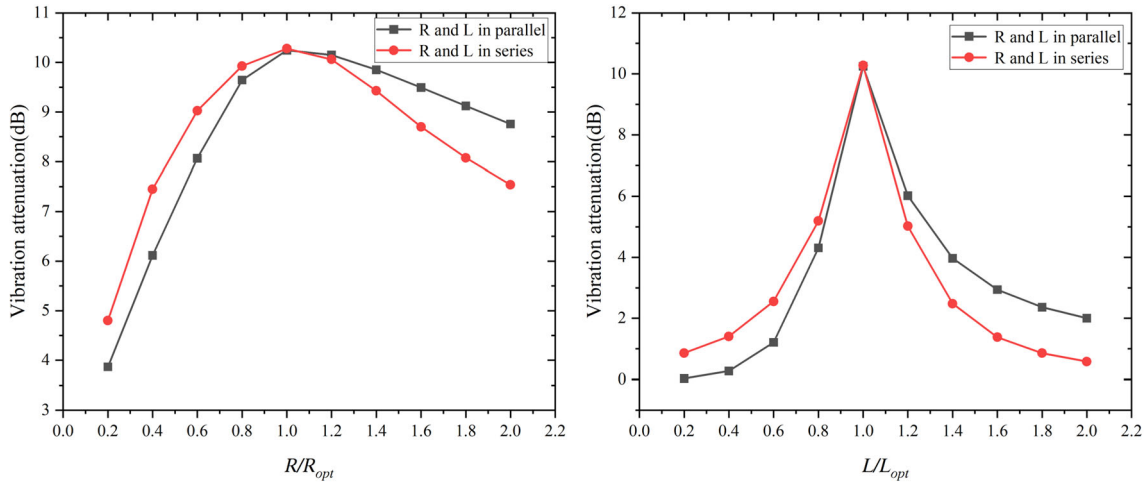
(a) Attenuation of vibration caused by the change of R (b) Attenuation of vibration caused by the change of L

Fig. 13 Vibration attenuation caused by the change of R and L in series and parallel circuits
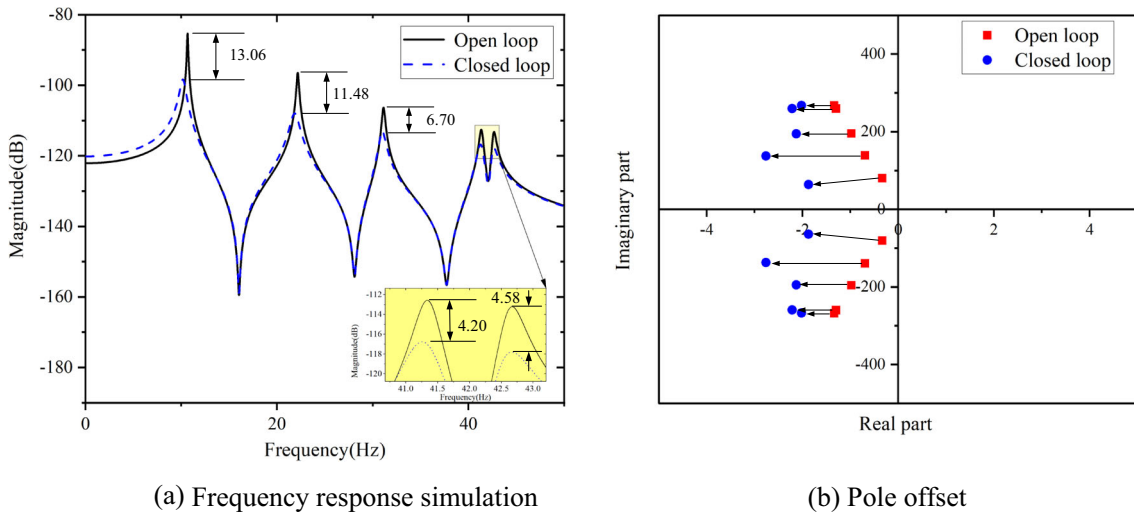
(a) Frequency response simulation   (b) Pole offset

Fig. 14 Frequency response and pole offset of open-loop system and closed-loop system

Finally, a comparison is conducted to assess the amplitude reduction of kinetic energy among the three fundamental circuits in near the first-order natural frequency, considering only the first-order mode. The component parameter values for all circuits have been optimized using the improved SCA algorithm, and the corresponding results are presented in Table 3. Analysis of Table 3 reveals that the utilization of a series connection of negative capacitance and resistance yields a greater reduction in kinetic energy compared to the other two circuits. Moreover, this configuration demonstrates the ability to effectively suppress vibrations associated with multiple order modes, as depicted in Fig. 14. However, it should be noted that the implementation cost associated with the series circuit comprising a negative capacitor and resistor is higher than that of the other two circuits. In practical applications, a combination of the three fundamental circuits can be employed to achieve more efficient vibration suppression.

Table 3 Kinetic energy amplitude reduction of the three circuits near the first-order natural frequency

Circuit	Component parameter values			Kinetic energy reduction (dB)
	Resistance (Ohm)	Inductance (Hy)	Negative capacitance (F)	
Resistance and inductance in parallel	129,125	345	–	11.1487
Resistance and inductance in series	4454	333	–	11.2132
Negative capacitance in series with resistance	135	–	6.4×10^{-7}	13.0600

4 Conclusions

This paper introduces a novel optimization algorithm and criteria for optimizing the parameters of piezoelectric transducer circuit components, with the goal of effectively suppressing bending vibrations in flexible structures. Firstly, a theoretical investigation is conducted on the commonly used parallel, series, and negative capacitive impedance circuits. Detailed derivations establish the response relationship between external excitation, rectangular plate displacement, and piezoelectric induced voltage. Additionally, the coupled dynamic model and transfer function model of the composite system are obtained. Next, evaluation criteria for bending vibration suppression are formulated by solving the system's frequency response and kinetic energy power spectrum. The SCA algorithm is further optimized through various enhancements, including improvements in the update direction and step size of the optimization solution. Moreover, the inclusion of inertia weight is employed to optimize the convergence speed of the solution. Furthermore, an action factor is introduced to reduce fluctuation around the optimal solution during the later stages of the algorithm. These optimizations significantly enhance the global search ability and local development accuracy of the algorithm.

The accuracy of the derived dynamic model and transfer function model is verified using the commercial finite element simulation software Workbench. Response analysis of the system is performed under various parameter values, damping conditions, and excitations. Furthermore, optimization calculations are conducted to determine the component parameter values in an example circuit. The obtained calculation results are then compared with those obtained using the previous method. This comparative analysis serves to validate the effectiveness and advantages of the proposed algorithm in optimizing the component parameter values in the shunt piezoelectric damping circuit.

Data availability All data that support the findings of this study are included within the article (and any supplementary files).

Declarations

Conflict of interest The authors declared no potential conflicts of interest with respect to the research, authorship, and/or publication of this article.

References

1. Berardengo, M., Cigada, A., Manzoni, S., Vanali, M.: Vibration control by means of piezoelectric actuators shunted with LR impedances: performance and robustness analysis. Shock Vib. **2015**, 1–30 (2015). https://doi.org/10.1155/2015/704265
2. Raze, G., Dietrich, J., Kerschen, G.: Passive control of multiple structural resonances with piezoelectric vibration absorbers. J. Sound Vib. **515**, 116490 (2021). https://doi.org/10.1016/j.jsv.2021.116490
3. Aridogan, U., Basdogan, I., Erturk, A.: Analytical modeling and experimental validation of a structurally integrated piezoelectric energy harvester on a thin plate. Smart Mater. Struct. **23**(4), 45039 (2014). https://doi.org/10.1088/0964-1726/23/4/045039
4. Yan, B., Wang, K., Hu, Z., Wu, C., Zhang, X.: Shunt damping vibration control technology: a review. Appl. Sci. **7**(5), 494 (2017). https://doi.org/10.3390/app7050494
5. Gripp, J.A.B., Rade, D.A.: Vibration and noise control using shunted piezoelectric transducers: a review. Mech. Syst. Signal Pr. **112**, 359–383 (2018). https://doi.org/10.1016/j.ymssp.2018.04.041

6. Safaei, M., Sodano, H.A., Anton, S.R.: A review of energy harvesting using piezoelectric materials: state-of-the-art a decade later (2008–2018). Smart Mater. Struct. **28**(11), 113001 (2019). https://doi.org/10.1088/1361-665X/ab36e4
7. Marakakis, K., Tairidis, G.K., Koutsianitis, P., Stavroulakis, G.E.: Shunt piezoelectric systems for noise and vibration control: a review. Front. Built Environ. (2019). https://doi.org/10.3389/fbuil.2019.00064
8. Fleming, A.J., Moheimani, S.O.R.: Control orientated synthesis of high-performance piezoelectric shunt impedances for structural vibration control. IEEE T. Contr. Syst. T. **13**(1), 98–112 (2005). https://doi.org/10.1109/TCST.2004.838547
9. Bo, L.D., He, H., Gardonio, P., Li, Y., Jiang, J.Z.: Design tool for elementary shunts connected to piezoelectric patches set to control multi-resonant flexural vibrations. J. Sound Vib. **520**, 116554 (2022). https://doi.org/10.1016/j.jsv.2021.116554
10. Ducarne, J., Thomas, O., Deü, J.F.: Placement and dimension optimization of shunted piezoelectric patches for vibration reduction. J. Sound Vib. **331**(14), 3286–3303 (2012). https://doi.org/10.1016/j.jsv.2012.03.002
11. Aridogan, U., Basdogan, I., Erturk, A.: Random vibration energy harvesting on thin plates using multiple piezopatches. J. Intel. Mat. Syst. Str. **27**(20), 2744–2756 (2016). https://doi.org/10.1177/1045389X16635846
12. Bricault, C., Pézerat, C., Collet, M., Pyskir, A., Perrard, P., Matten, G., Romero-García, V.: Multimodal reduction of acoustic radiation of thin plates by using a single piezoelectric patch with a negative capacitance shunt. Appl. Acoust. **145**, 320–327 (2019). https://doi.org/10.1016/j.apacoust.2018.10.016
13. Zhao, Y.: Vibration suppression of a quadrilateral plate using hybrid piezoelectric circuits. J. Vib. Control **16**(5), 701–720 (2010). https://doi.org/10.1177/1077546309106529
14. Ji, H., Guo, Y., Qiu, J., Wu, Y., Zhang, C., Tao, C.: A new design of unsymmetrical shunt circuit with negative capacitance for enhanced vibration control. Mech. Syst. Signal Pr. **155**, 107576 (2021). https://doi.org/10.1016/j.ymssp.2020.107576
15. Pohl, M.: Increasing the performance of negative capacitance shunts by enlarging the output voltage to the requirements of piezoelectric transducers. J. Intel. Mat. Syst. Str. **28**(11), 1379–1390 (2017). https://doi.org/10.1177/1045389X16666181
16. Berardengo, M., Thomas, O., Giraud-Audine, C., Manzoni, S.: Improved resistive shunt by means of negative capacitance: new circuit, performances and multi-mode control. Smart Mater. Struct. **25**(7), 75033–75055 (2016). https://doi.org/10.1088/0964-1726/25/7/075033
17. Soltani, P., Kerschen, G., Tondreau, G., Deraemaeker, A.: Piezoelectric vibration damping using resonant shunt circuits: an exact solution. Smart Mater. Struct. **23**(12), 125014 (2014). https://doi.org/10.1088/0964-1726/23/12/125014
18. Ducarne, J., Thomas, O., Deü, J.F.: Structural vibration reduction by switch shunting of piezoelectric elements: modeling and optimization. J. Intel. Mat. Syst. Str. **21**(8), 797–816 (2010). https://doi.org/10.1177/1045389X10367835
19. Ravi, S., Zilian, A.: Monolithic modeling and finite element analysis of piezoelectric energy harvesters. Acta Mech. **228**(6), 2251–2267 (2017). https://doi.org/10.1007/s00707-017-1830-7
20. Yamada, K., Matsuhisa, H., Utsuno, H., Sawada, K.: Optimum tuning of series and parallel LR circuits for passive vibration suppression using piezoelectric elements. J. Sound Vib. **329**(24), 5036–5057 (2010). https://doi.org/10.1016/j.jsv.2010.06.021
21. Wang, G., Lu, Y.: An improved lumped parameter model for a piezoelectric energy harvester in transverse vibration. Shock Vib. **2014**, 1–12 (2014). https://doi.org/10.1155/2014/935298
22. Høgsberg, J., Krenk, S.: Balanced calibration of resonant shunt circuits for piezoelectric vibration control. J. Intel. Mat. Syst. Str. **23**(17), 1937–1948 (2012). https://doi.org/10.1177/1045389X12455727
23. Gardonio, P., Zientek, M., Dal Bo, L.: Panel with self-tuning shunted piezoelectric patches for broadband flexural vibration control. Mech. Syst. Signal Pr. **134**, 106299 (2019). https://doi.org/10.1016/j.ymssp.2019.106299
24. Beck, B.S., Cunefare, K.A., Collet, M.: Response-based tuning of a negative capacitance shunt for vibration control. J. Intel. Mat. Syst. Str. **25**(13), 1585–1595 (2014). https://doi.org/10.1177/1045389X13510216
25. Toftekær, J.F., Benjeddou, A., Høgsberg, J.: General numerical implementation of a new piezoelectric shunt tuning method based on the effective electromechanical coupling coefficient. Mech. Adv. Mater. Struc. **27**(22), 1908–1922 (2020). https://doi.org/10.1080/15376494.2018.1549297
26. Heuss, O., Salloum, R., Mayer, D., Melz, T.: Tuning of a vibration absorber with shunted piezoelectric transducers. Arch. Appl. Mech. **86**(10), 1715–1732 (2016). https://doi.org/10.1007/s00419-014-0972-5
27. Lumentut, M.F., Howard, I.M.: Effect of shunted piezoelectric control for tuning piezoelectric power harvesting system responses-analytical techniques. Smart Mater. Struct. **24**(10), 105029 (2015). https://doi.org/10.1088/0964-1726/24/10/105029
28. Mirjalili, S.C.A.: A Sine Cosine Algorithm for solving optimization problems. Knowl. Based Syst. **96**, 120–133 (2016). https://doi.org/10.1016/j.knosys.2015.12.022
29. Donoso, A., Bellido, J.C.: Robust design of multimodal piezoelectric transducers. Comput. Method. Appl. M. **338**, 27–40 (2018). https://doi.org/10.1016/j.cma.2018.04.016
30. Liao, Y., Liang, J.: Unified modeling, analysis and comparison of piezoelectric vibration energy harvesters. Mech. Syst. Signal Pr. **123**, 403–425 (2019). https://doi.org/10.1016/j.ymssp.2019.01.025
31. Behrens, S., Fleming, A.J., Moheimani, S.O.R.: A broadband controller for shunt piezoelectric damping of structural vibration. Smart Mater. Struct. **12**(1), 18–28 (2003). https://doi.org/10.1088/0964-1726/12/1/303
32. Gardonio, P., Casagrande, D.: Shunted piezoelectric patch vibration absorber on two-dimensional thin structures: tuning considerations. J. Sound Vib. **395**, 26–47 (2017). https://doi.org/10.1016/j.jsv.2017.02.019
33. Yıldız, B.S., Yıldız, A.R.: Comparison of grey wolf, whale, water cycle, ant lion and sine-cosine algorithms for the optimization of a vehicle engine connecting rod. Mater. Test. **60**(3), 311–315 (2018). https://doi.org/10.3139/120.111153